Applied Catalysis B: Environmental 168-169 (2015) 243–249

Contents lists available at ScienceDirect

Applied Catalysis B: Environmental

journal homepage: www.elsevier.com/locate/apcatb

Effective mineralization of organic dye under visible-light irradiation over electronic-structure-modulated $Sn(Nb_{1-x}Ta_x)_2O_6$ solid solutions

Jian Ren[a], Shuxin Ouyang[a,b,c,*], Hungru Chen[d], Naoto Umezawa[d], Da Lu[a], Defa Wang[a,b,c,**], Hua Xu[a,b,c], Jinhua Ye[a,b,d]

[a] TU-NIMS Joint Research Center, School of Materials Science and Engineering, Tianjin University, 92 Weijin Road, Nankai District, Tianjin 300072, PR China
[b] Collaborative Innovation Center of Chemical Science and Engineering (Tianjin), Tianjin 300072, PR China
[c] Tianjin Key Laboratory of Composite and Functional Materials, and Key Lab of Advanced Ceramics and Machining Technology, Ministry of Education, Tianjin 300072, PR China
[d] Environmental Remediation Materials Unit, and International Center for Materials Nanoarchitectonics (MANA), National Institute for Materials Science (NIMS), 1-1 Namiki, Tsukuba 305-0044, Japan

ARTICLE INFO

Article history:
Received 14 October 2014
Received in revised form 9 December 2014
Accepted 14 December 2014
Available online 17 December 2014

Keywords:
Photocatalysis
Solid solution
Dye photodgradation
Mineralization
Electronic structure

ABSTRACT

A series of $Sn(Nb_{1-x}Ta_x)_2O_6$ solid solutions were successfully synthesized as novel visible-light-active photocatalysts. The characterizations of powder X-ray diffraction and UV–vis absorption spectrum indicate that these solid solutions possess continuous changes in the crystallography features and optical band gaps, and are therefore a group of continuous solid solutions. Their photocatalytic properties were evaluated via methylene blue (MB) photodegradation. The $Sn(Nb_{0.8}Ta_{0.2})_2O_6$ sample showed the best photocatalytic performance, full mineralization ability, and an excellent stability. After 120 min of irradiation, the degradation and mineralization percentages of MB over $Sn(Nb_{0.8}Ta_{0.2})_2O_6$ reached 99.5% and 98.9%, respectively; in addition, the degradation ratio remained at 97% after five-cyclic test. The further study on the active species and the theoretical calculation based on density functional theory helped to clarify the mechanism of the photodegradation reaction. On this basis, we propose the strategies to design high-performance photocatalysts employed in hole-dominated and electron-dominated photocatalytic applications, respectively.

1. Introduction

With the high-speed economic growth, the amounts of pollutants discharge and energy consumption have increased sharply over the past decades. Semiconductor-based photocatalysis as an environment-friendly technology has attracted wide attention since it supplies a potential solution to the worldwide environmental pollution and energy shortage [1–3]. TiO_2 is especially promising as one of stable, nontoxic, and low-cost photocatalysts, but the sparse light absorption makes it work only under the UV light irradiation, and thus, restricts its widespread application [4,5]. It is crucial for a photocatalytic process to harness the abundant solar energy, both UV light and visible light. To achieve the goal, much effort has been expended to develop highly visible-light-active photocatalysts. Second-generation TiO_2-based catalysts are developed successfully by using doping with transition-metal cations [6,7] or anions (e.g., N, C, and S) [8–10]. However, these modifications improved little in organic compounds mineralization. Energy band engineering supplies an effective approach to explore visible-light-sensitive photocatalysts with high performance via adjusting the valence band (VB), [11–13] modifying the conduction band (CB), [14–16] or continuous modulating the CB, VB, or both, [17] which simultaneously suppresses the redox potentials. Thus, fabrication of solid solution photocatalysts with continuous band gap has emerged as a requirement. Interestingly and importantly, the derived advantageous performances in the solid-solution photocatalysts are unattainable by the individual end material [18–22].

AM_2O_6 (M = Nb, Ta) oxide photocatalysts have been extensively studied by many researchers since 1998. At first, these materials were used for water splitting under UV irradiation [23,24]. Then, Ye and Zou developed a new kind of visible-light-sensitive

* Corresponding author at: TU-NIMS Joint Research Center, School of Materials Science and Engineering, Tianjin University, 92 Weijin Road, Nankai District, Tianjin 300072, PR China. Tel.: +86 2227409157.
** Corresponding author at: TU-NIMS oint Research Center, School of Materials Science and Engineering, Tianjin University, 92 Weijin Road, Nankai District, Tianjin 300072, PR China.
E-mail addresses: oysx@tju.edu.cn (S. Ouyang), defawang@tju.edu.cn (D. Wang).

http://dx.doi.org/10.1016/j.apcatb.2014.12.021
0926-3373/

Table 1
Mineralization abilities of some typical photocatalysts.

Material	Reaction conditions	Organic dye[a]	MP[b]	Refs.
TiO_2	$\lambda \geq 340$ nm, 125 W high pressure mercury lamp, 6 h	MB	80%	[4]
Ag_2GeO_3	$\lambda \geq 310$ nm, 18 W white fluorescent lamp, 2.5 h	MB	79%	[13]
$AgPO_3$	$\lambda \geq 400$ nm, 300 W Xe lamp, 10 min	MB	60%	[16]
$SnNb_2O_6$	$\lambda \geq 420$ nm, 300 W Xe lamp, 3.5 h	RhB	15%	[31]
Bi_2WO_6	$\lambda \geq 420$ nm, 500 W Xe lamp, 20 h	RhB	92%	[32]
$BiVO_4$	$\lambda \geq 420$ nm, 500 W Xe lamp, 4.5 h	RhB	22%	[33]
BiOCl	$\lambda \geq 365$ nm, 250 W ultraviolet lamp, 8 h	MO	75%	[34]

[a] MB: methylene blue, RhB: rhodamine B, MO: methyl orange.
[b] MP: mineralization percentage.

photocatalysts $NiNb_2O_6$ and $NiTa_2O_6$, which can achieve the solar-driven hydrogen evolution from pure water without any co-catalyst [25,26]. After that, these Nb- or Ta-contained photocatalysts were employed in the application of environmental remediation and have aroused wide interest [27–31]. However, the solid-solution photocatalysts of AM_2O_6 type have not been investigated yet.

Although it has taken a lot of effort to develop new visible-light-active materials for environmental purification, few of them have attained the adequate ability for effective mineralization of organic dye (see Table 1) [4,13,16,31–34]. In this study, a novel series of $Sn(Nb_{1-x}Ta_x)_2O_6$ ($0 \leq x \leq 1$) solid-solution photocatalysts were synthesized, which exhibited visible-light-sensitive activities for methylene blue mineralization. Among them, after 120 min of irradiation, the degradation and mineralization percentages of MB over $Sn(Nb_{0.8}Ta_{0.2})_2O_6$ reached 99.5% and 98.9%, respectively; more importantly, the degradation ratio remained at 97% after five-cycle test. Then, the active species involved in this process and the theoretical calculation of electronic structure were systematically studied. Furthermore, a feasible and effective strategy of designing high-active photocatalysts is proposed.

2. Experimental

2.1. Material preparation

$Sn(Nb_{1-x}Ta_x)_2O_6$ ($0 \leq x \leq 1$) solid solutions were prepared via the solid-state reaction. The reactants SnO (Sinopharm Chemical, 99.99%), Nb_2O_5 (Sinopharm Chemical, 99.9%), and Ta_2O_5 (Sinopharm Chemical, 99.9%) in stoichiometric ratios were weighed out and thoroughly ground with addition of ethanol. The well mixed precursors were located in an alumina boat and heated at 900 °C for 2 h under flowing nitrogen atmosphere.

2.2. Sample characterization

The crystal structures of the as-synthesized solid solutions were characterized by powder X-ray diffraction (Rigaku, D/MAX 2500) with Cu $K\alpha_1$ radiation. The diffuse reflectance spectra were measured using a UV–vis-NIR spectrometer with an integrating sphere (Shimadzu, UV-3600) and were converted to the absorption spectra by the Kubelka–Munk method. A field emission scanning electron microscope (FE-SEM, Hitachi S-4800) and a high-resolution transmission electron microscope (HRTEM, JEOL JEM-2100F, operated at 200 kV), both of which were equipped with an energy-dispersive spectrometer (EDS), were employed for morphology observation and composition analysis.

2.3. Activity evaluation

The photocatalytic activities of the $Sn(Nb_{1-x}Ta_x)_2O_6$ ($0 \leq x \leq 1$) solid solutions were evaluated by the degradation of methylene blue (MB) under a 300 W Xe illuminator (CEL-HXF300, CEAULIGHT) equipped with a cutoff filter (UVIRCUT420, CEAULIGHT) ($\lambda \geq 420$ nm). MB is chosen as the model pollutant since its photodegradation over the $Sn(Nb_{1-x}Ta_x)_2O_6$ solid-solution photocatalysts is mainly governed by the intrinsic photocatalytic process (the photodegradation experiment under monochromatic light of 425 nm is shown in Supporting information, Fig. S1). In a typical process, 0.1 g photocatalyst powders were dispersed in 100 mL MB (10 mg L^{-1}) solution by a magnetic stirrer in a cell. Before irradiation, the suspension was stirred in the dark for 60 min to reach the adsorption–desorption equilibrium of MB. Then, the suspension was irradiated with visible light. After a certain time interval (20 min), 3 mL of the solution was sampled, and the catalyst was separated from the solution by centrifugation to obtain a clear liquid. The concentrations and the mineralization percentages of organic dye were measured by a UV–vis spectrophotometer (Shimadzu, UV-2700) and a TOC analyzer (Shimadzu, TOC-LCPH), respectively.

2.4. Mechanism study

Typical active species in photocatalytic reaction, such as holes, electrons, hydroxyl radical ($^{\bullet}OH$), and superoxide anion radicals ($^{\bullet}O_2^-$) can be investigated using different types of active-species scavengers. In this study, *t*-butyl alcohol (TBA), *p*-benzoquinone (PBQ), and ammonium oxalate (AO) were added to the reaction solutions as $^{\bullet}OH$ [35], $^{\bullet}O_2^-$ [36] and hole [37] scavenger, respectively. A certain amount of scavengers were added into the MB solution prior to addition of catalysts. The following process of MB degradation was the same as Section 2.3.

2.5. Theoretical calculation

All calculations were performed using DFT with the GGA-PBE functional [38]. An additional Hubbard-*U* like term [39] has also been applied to Nb and Ta d orbitals (the DFT + *U* method). The interactions between core and valence electrons were treated with the projector augmented wave (PAW) method [40]. The valence electronic configurations for Sn, Ta, Nb, and O atoms were $5s^25p^2$, $6s^25d^3$, $5s^14d^4$, and $2s^22p^4$, respectively, which were described by a plane wave basis set with an energy cutoff of 500 eV. The *k*-space was sampled with a $2 \times 8 \times 7$ k-point mesh. For all calculated cells, the lattice vectors and atomic positions were allowed to relax until the force was converged to less than 0.03 eV/Å at each atomic position. All calculations were carried out using the Vienna Ab initio simulation package (VASP) [41].

3. Results and discussion

3.1. Crystal structure

Solid-state reaction was proven to be a facile and effective method to prepare solid-solution photocatalysts [20,42,43]. In this work, the photocatalysts were synthesized by calcining oxide precursors under N_2 protection, to avoid the oxidation of Sn^{II}. In

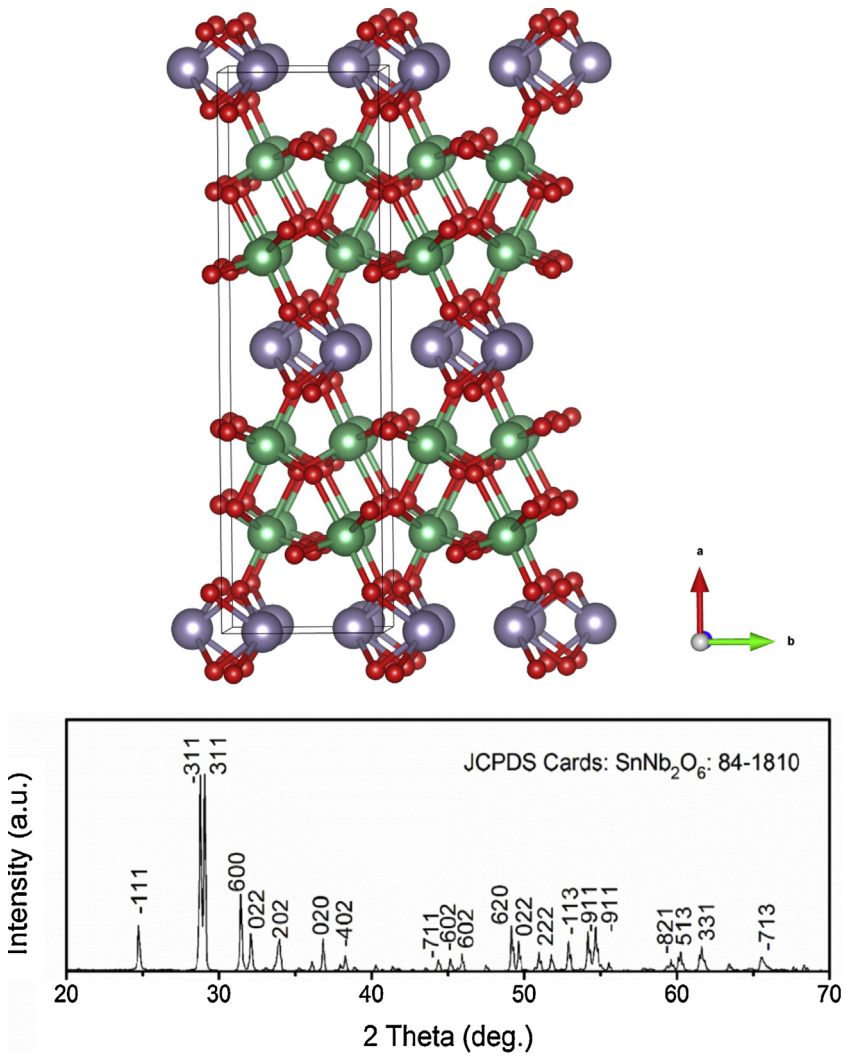

Fig. 1. Schematic crystal structure and XRD pattern of $SnNb_2O_6$.

the beginning, we synthesized $SnNb_2O_6$, which crystallizes as an AB_2O_6 oxide with typical Foordite structure. Fig. 1 exhibits the crystal structure and XRD pattern of $SnNb_2O_6$. In YZ plane, the NbO_4 tetrahedrons connect to each other to form zigzag chains by sharing vertexes; these chains of NbO_4 tetrahedrons construct a double layer without sharing any vertex or edge; the Sn-atom layers locate between these NbO_4-tetrahedronal double layers. Then, the $Sn(Nb_{1-x}Ta_x)_2O_6$ ($0 \le x \le 1$) solid solutions were prepared with the gradual substitution of Nb by Ta using the same method. Their XRD patterns are shown in Fig. 2. It could be clearly seen that all of the samples have a homogeneous crystal structure with monoclinic symmetry; however, as varying x from 0 to 1, all diffraction peaks gradually shift to bigger angles. The enlarged patterns from 28.5° to 29.5° reveal a continuous shift of the diffraction peaks which represent the crystal plane (−3 1 1) and (3 1 1). The XRD patterns were also used to deduce the lattice parameters of these solid solutions, which are shown in Table 2. Obviously, with varying x from 0 to 1, the lattice constants (a, b, c) and angle β decrease gradually, indicating the as-prepared samples are a group of continuous solid solutions.

3.2. Morphology and photophysical property

The morphologies of the solid solutions were observed by field emission scanning electron microscopy (FE-SEM). The SEM images of as-prepared samples are shown in Fig. 3. The photocatalysts are all irregular particles agglomerated by a lot of crystallites with the particle size in the range of 200–600 nm. Besides, morphological changed little with increasing the amount of Ta. The equipped (EDS) probed the chemical compositions of these samples. The results

Table 2
Lattice parameters and band gaps of $Sn(Nb_{1-x}Ta_x)_2O_6$.

Sample	x	a (Å)	b (Å)	c (Å)	α (°)	β (°)	γ (°)	E_g (eV)
$SnNb_2O_6$	0	17.11	4.89	5.58	90.0	91.02	90.0	2.25
$Sn(Nb_{0.8}Ta_{0.2})_2O_6$	0.2	17.08	4.87	5.57	90.0	90.99	90.0	2.31
$Sn(Nb_{0.6}Ta_{0.4})_2O_6$	0.4	17.06	4.87	5.56	90.0	90.96	90.0	2.42
$Sn(Nb_{0.4}Ta_{0.6})_2O_6$	0.6	17.05	4.86	5.55	90.0	90.94	90.0	2.52
$Sn(Nb_{0.2}Ta_{0.8})_2O_6$	0.8	17.04	4.86	5.55	90.0	90.93	90.0	2.64
$SnTa_2O_6$	1	17.03	4.85	5.54	90.0	90.91	90.0	2.73

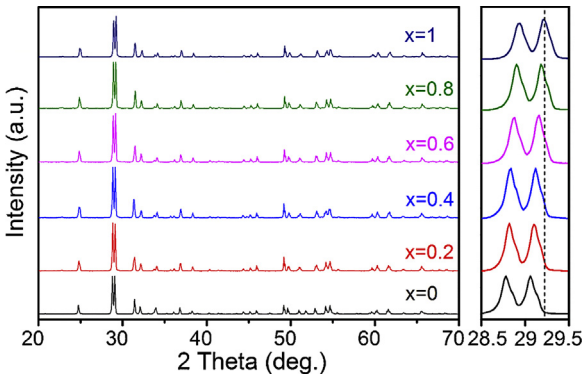

Fig. 2. XRD patterns of $Sn(Nb_{1-x}Ta_x)_2O_6$ solid solutions (JCPDS cards: $SnNb_2O_6$: 84-1810; $SnTa_2O_6$: 87-0358).

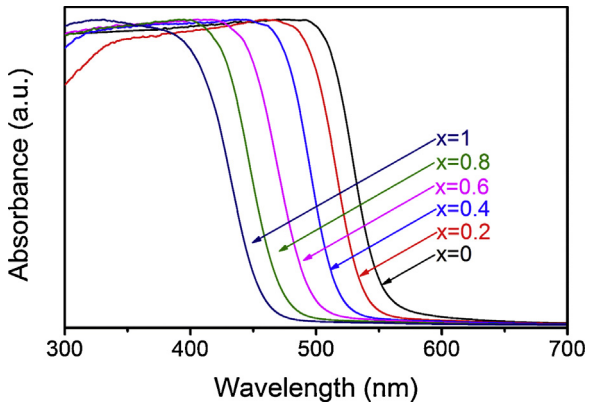

Fig. 4. UV–vis absorption spectra of $Sn(Nb_{1-x}Ta_x)_2O_6$ solid solutions.

revealed the gradual change in the amount of Nb and Ta (for details see Supporting information, Fig. S2 and Table S1), indicating that the as-prepared samples are a group of continuous solid solutions.

As shown in Fig. 4, the UV–vis absorption spectra of the as-prepared samples possess steep edges in the profiles, indicating that the visible-light response of the solid solutions is not caused by impurity level but by band gap transitions from VB to CB. The band gaps of $SnNb_2O_6$ and $SnTa_2O_6$ were estimated to be 2.25 and 2.73 eV from the onsets of the absorption edges, respectively, which are rationally in accordance with previous reports [44]. The absorption edges of the $Sn(Nb_{1-x}Ta_x)_2O_6$ solid solutions were notably located between those of $SnNb_2O_6$ and $SnTa_2O_6$, and the absorption spectra were blue-shifted monotonically as Nb was gradually substituted with Ta. The band gaps of the $Sn(Nb_{1-x}Ta_x)_2O_6$ solid solutions were estimated to be 2.25–2.73 eV(as shown in Table S2). All the results as above-presented confirm that the as-prepared powders were a group of continuous solid solutions rather than the mixtures of $SnNb_2O_6$ and $SnTa_2O_6$.

3.3. Photocatalytic property and mechanism

The photocatalytic activities of $Sn(Nb_{1-x}Ta_x)_2O_6$ solid solutions were evaluated via the MB photodegradation under visible light irradiation. Fig. 5(a) presents the changes of MB concentration over these photocatalysts. The MB degradation with photocatalysts all reached more than 75% after 120 min of irradiation. However, a contrast experiment without any photocatalyst under the same conditions showed that MB self-photolysis was only 36%. As can be seen from Fig. 5(b), the photodegradation process is fit for pseudo first-order kinetics by linear fitting according to $\ln(C_0/C_t) = kt$, where C_0 is the initial concentration of MB at adsorption/desorption equilibrium, C_t is the concentration of MB at time t. The apparent rate constants and the mineralization percentages are plotted in Fig. 5(c), which indicates a close dependence on the chemical compositions of $Sn(Nb_{1-x}Ta_x)_2O_6$ solid solutions. With varying x from 0 to 0.2, the photocatalytic activity increased, then it goes down as x continues to increase from 0.2 to 1.0. Among this series of solid solutions, the $Sn(Nb_{0.8}Ta_{0.2})_2O_6$ showed the best performance.

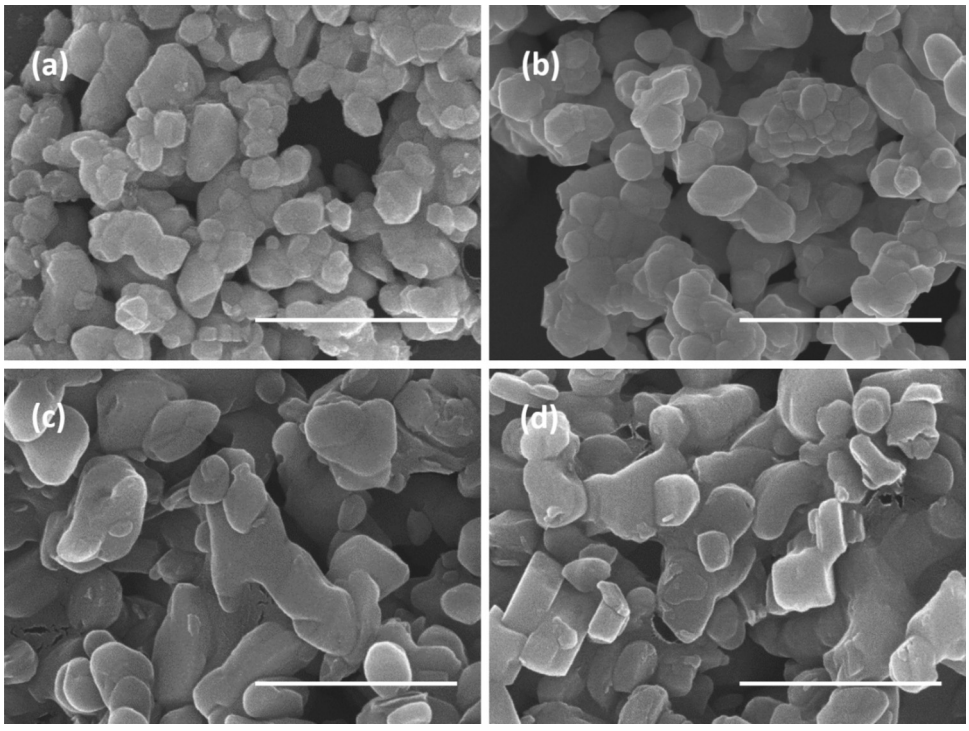

Fig. 3. SEM images of the as-prepared samples, (a) $SnNb_2O_6$, (b) $Sn(Nb_{0.8}Ta_{0.2})_2O_6$, (c) $Sn(Nb_{0.2}Ta_{0.8})_2O_6$, and (d) $SnTa_2O_6$, the scale bar is 1 μm.

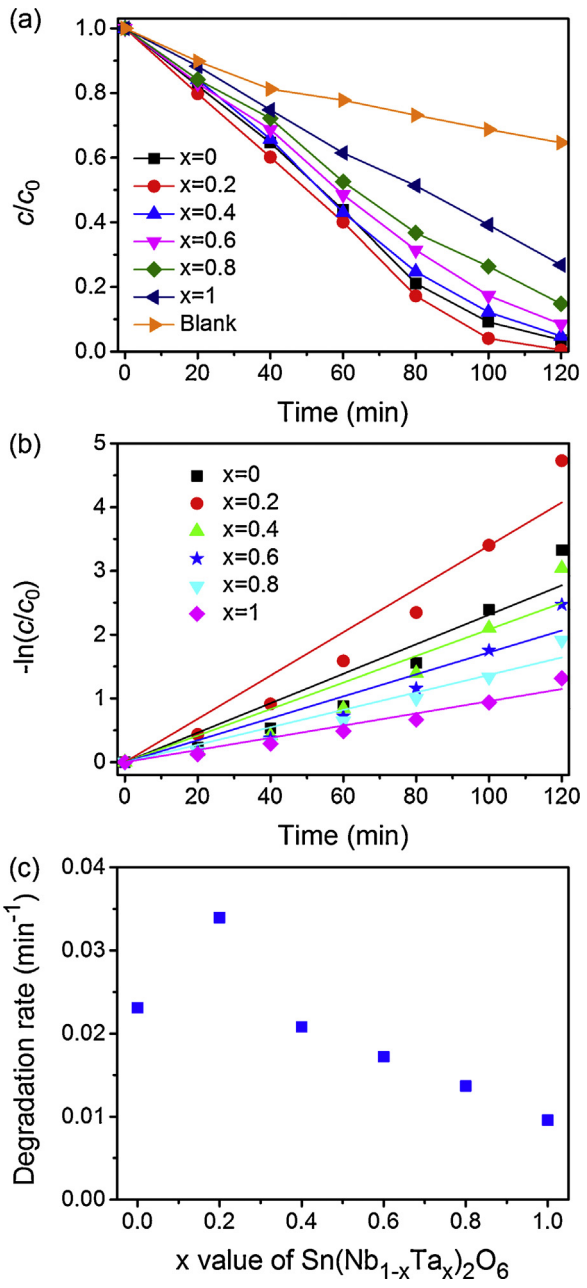

Fig. 5. Photocatalytic degradation of MB over $Sn(Nb_{1-x}Ta_x)_2O_6$ solid solutions under visible-light irradiation ($\lambda \geq 420$ nm). (a) Concentration changes of MB solution, (b) kinetic linear fitting of the concentration changes, and (c) degradation rates and mineralization capabilities of $Sn(Nb_{1-x}Ta_x)_2O_6$ solid solutions.

Next, to study the reaction stability, a five-cycle MB photodegradation test under visible-light irradiation was conducted over $Sn(Nb_{0.8}Ta_{0.2})_2O_6$. As displayed in Fig. 6, after five-cycle photodegradation, the degradation ratio of MB remained 97%. The XRD patterns and UV–vis absorption spectra of the samples before and after reaction indicate no obvious changes of the crystal structure and light-absorption property over this photocatalyst during the photodegradation reaction (see details in Supporting information, Fig. S3).

Many studies about the high stability of dye photodegradation over various photocatalysts have been reported [25–27]; however, most of them did not explain the original reason. As we know that catalytic reactions are correlated to the active sites on the catalyst surface. The catalysts will be passivation if the active sites are covered with intermediate [45]. Therefore, it is speculated that a high stability of photocatalyst requires relatively completed mineralization to the organic contaminant. The photodegradation over $Sn(Nb_{0.8}Ta_{0.2})_2O_6$ under visible light illumination did achieve a complete mineralization of MB without organic residues. This opinion could be supported by the dramatic decrease of the intensity of the bands at 245 and 296 nm due to the $^1L_a \longleftarrow {}^1A$ and $^1L_b \longleftarrow {}^1A$ transitions of the phenyl moieties in the UV–vis absorption spectra of MB solutions (see details in Supporting information, Fig. S4). Additionally, from the TOC measurements, the total organic carbon concentration ([TOC]) could be obtained, and then the mineralization percentage (MP) could be deduced by the equation as below.

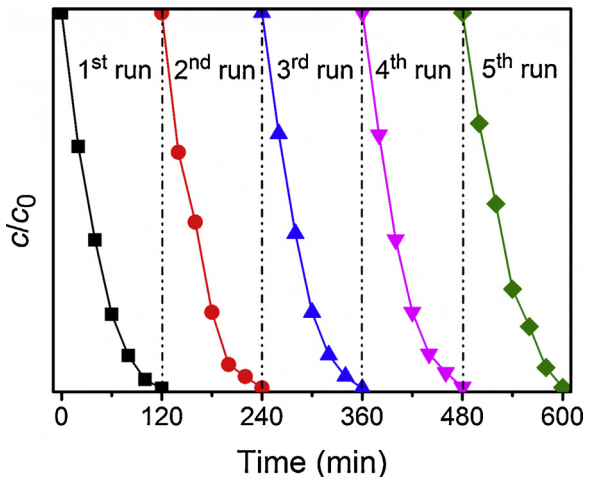

Fig. 6. Cyclic tests of the 120-min-period experiment of MB decomposition over $Sn(Nb_{0.8}Ta_{0.2})_2O_6$.

$$MP = \frac{[TOC]_0 - [TOC]_t}{[TOC]_0} \times 100\%$$

For $Sn(Nb_{0.8}Ta_{0.2})_2O_6$, MP = 98.9% after photodegradation, which means only about 1% of TOC still remained in the solution after 120 min of irradiation (the experimental data are shown in Supporting information, Table S2).

It is interesting to explore the reason about the high mineralization capability over the $Sn(Nb_{0.8}Ta_{0.2})_2O_6$ photocatalyst. We, therefore, further studied the active species in the MB photodegradation over this photocatalyst and the results were shown in Fig. 7. As aforementioned, without the addition of scavengers, the degradation of MB was up to 99.5% after 120 min of irradiation. However,

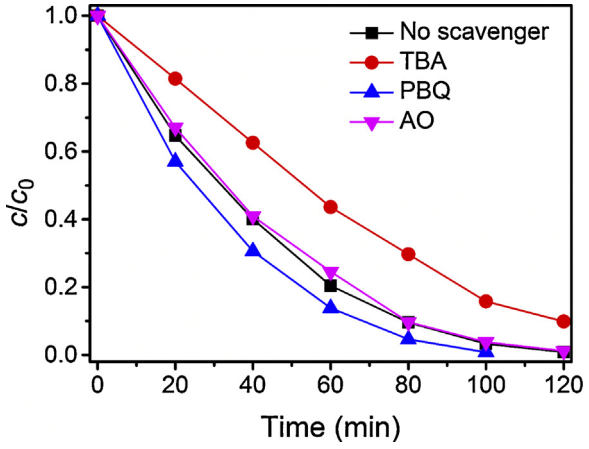

Fig. 7. Photocatalytic degradation of MB over $Sn(Nb_{0.8}Ta_{0.2})_2O_6$ under visible-light irradiation ($\lambda \geq 420$ nm) using different scavengers.

after adding 5 mL of TBA as the capturer of •OH, the degradation ratio of MB was reduced to about 80% after 120 min of irradiation, indicating that the •OH plays a crucial role in this photocatalytic reaction. After 10 mg of AO as a hole-scavenger were added into the reaction system, the degradation rate of MB changed little. It reveals that once the holes are generated, it will react with the surface hydroxyl groups or the adsorbed water to produce •OH. After 10 mg of PBQ was introduced to the reaction solution to quench $^{\bullet}O_2^-$ which could be produced by O_2 molecular accepting electrons, the photocatalytic conversion accelerated rapidly. This may attribute to that the trap of electrons facilitates the separation of photoinduced carriers, and thus, increase the possibility of holes combining with OH^- to generate •OH. Additionally, the reactions operated under different conditions, such as N_2 bubbled and O_2 bubbled cases, validated the speculation powerfully (see detail in Supporting information, Fig. S5). To evidence the •OH can be generated over the photocatalyst, the water photooxidization to produce O_2 under visible-light irradiation was measured for the $Sn(Nb_{0.8}Ta_{0.2})_2O_6$ sample (refer to Supporting information, Fig. S6). The generation reactions mentioned above are proposed in the following.

$$OH^- + h_{VB}{}^+ \rightarrow HO^{\bullet}$$

$$HO^{\bullet} + MB \rightarrow CO_2 + H_2O$$

$$O_2 + e_{CB}{}^- \rightarrow {}^{\bullet}O_2^-$$

Through the discussion above, the MB photocatalytic oxidation was driven mainly by the participation of •OH radicals with the assistance of holes and dissolved O_2.

3.4. Band structures of $Sn(Nb_{1-x}Ta_x)_2O_6$ solid solutions

The electronic structure of a semiconductor material plays a crucial role in its functional properties. As above discussed, the photocatalytic decomposition of MB over $Sn(Nb_{0.8}Ta_{0.2})_2O_6$ in the presence of O_2 generally involves: (1) photoexcitation of electrons from VB to CB, (2) oxidation of MB by the •OH generated by holes combining with OH^-, and (3) reduction of O_2 by the CB electrons. Thermodynamically, increasing the over-potentials, which are the difference between the energy levels of valence band minimum (VBM) and oxidation potential (E_{ox}), and between the energy levels of conduction band maximum (CBM) and reduction potential (E_{red}), are clearly favorable for the redox reactions.

To clarify the effect of the x value to the electronic structures and the photocatalytic activities, the band structures of $Sn(Nb_{1-x}Ta_x)_2O_6$ solid solutions were studied, while $x = 0$, 0.5, and 1 were enough to exhibit the trend of the changes (more details in Supporting information, Note 1, Figs. S7 and S8). Fig. 8(a) shows the densities of states (DOS) of $SnNb_2O_6$, $SnNbTaO_6$, and $SnTa_2O_6$ under the $U = 4$ eV, which illustrates that the levels of VBM all consist of Sn 5s5p and O 2p orbitals and thus are similar, but the levels of CBM are changed by the ratio of Ta/Nb ($U = 0$ and $U = 7$ eV were also applied in the calculation, and the similar results are shown in Supporting infomation, Fig. S9). As discussed in the Section 3.2, the photodegradation of MB is a hole-dominated reaction, controlled by the position of VBM, what the role does the modulated CBM play in the optimization of photodegradation activity?

Fig. 8(b) shows the partial density of states (PDOS), corresponding to the CBM region in Fig. 8(a). It is clear that the CBM are mainly formed by the Nb 4d and Ta 5d orbitals. Since Nb 4d levels are lower than Ta 5d levels, the substitution of Nb by Ta induces a negative shift of CBM and subsequently broadens the band gap. On the basis of the band structure characteristics of the present solid solutions, the higher level of CBM strengthens the reduction ability, but narrows light absorption range in the visible region.

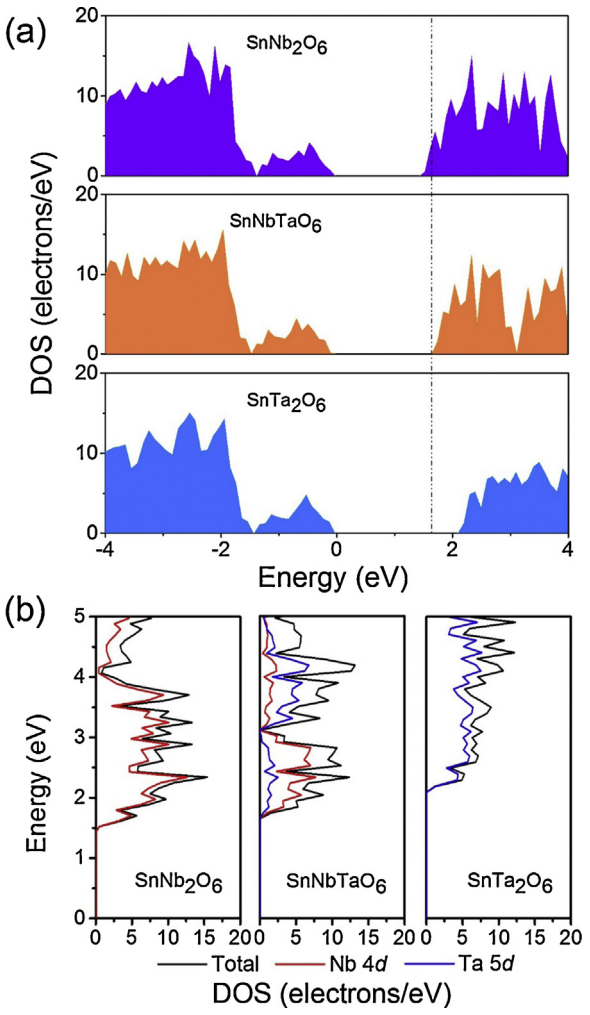

Fig. 8. Density of states of $Sn(Nb_{1-x}Ta_x)_2O_6$ ($x = 0$, 0.5, and 1) under $U = 4$ eV.

Therefore, a certain amount of substitution of Nb by Ta could enhance the reductive potential, which is beneficial for electron combining with O_2 and thus increase photodegradation activity of MB; however, the excess substitution of Nb by Ta will reduce the light absorption and thus weaken the catalytic activity. Due to a good balance between the effective visible-light absorption and adequate redox potentials, the $Sn(Nb_{0.8}Ta_{0.2})_2O_6$ attained an optimal band structure, which contributes to the best photocatalytic activity. The calculation results are consistent with the variation of the optical band gaps, although the gap between the highest occupied and lowest unoccupied states in our LDA + U scheme was smaller than that obtained experimentally, which could be ascribed to the limitation of DFT [46].

By combining the experimental and theoretical investigations, a feasible and effective strategy of designing high visible-light active photocatalysts based on solid-solution systems could be summarized. As presented in Fig. 9, aiming at the development of high performance photocatalysts applying in the process dominated by electrons, including splitting water into H_2, photocatalytic destruction of gaseous organic pollutants and reduction of metal ions under irradiation in aqueous solution, the methodology of energy band engineering requires a steady CB level to guarantee a strong reduction potential, the light absorption could be extended into the visible region through adjusting the VB. On the contrary, the photocatalysts used in the hole-dominated photoreaction, such as photocatalytic water oxidation to form O_2, and oxidation of organic compounds in liquid phase, should possess a similar VB level, and

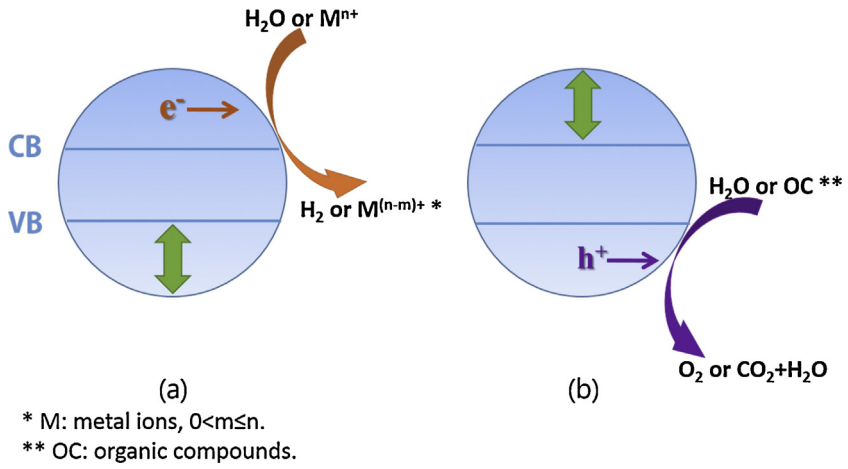

Fig. 9. Strategies to design photocatalysts applying in (a) electron-dominated and (b) hole-dominated reactions.

the photocatalytic performances could be enhanced by modulating the CB continuously.

4. Conclusions

A new series of $Sn(Nb_{1-x}Ta_x)_2O_6$ $(0 \le x \le 1)$ solid-solution photocatalysts were synthesized by solid-state reactions. All of these solid solutions possessed visible-light photoactivities for the MB degradation. The photocatalytic efficiency was closely depended on the x value in $Sn(Nb_{1-x}Ta_x)_2O_6$ $(0 \le x \le 1)$. Among them, the $Sn(Nb_{0.8}Ta_{0.2})_2O_6$ sample showed the highest catalytic efficiency, achieved a full mineralization and exhibited an excellent stablity. Under 120 min of visible-light irradiation, the degradation and mineralization percentages of MB over $Sn(Nb_{0.8}Ta_{0.2})_2O_6$ was up to 99.5% and 98.9%, respectively. The study of photocatalytic mechanism revealed that the MB photodegradations over $Sn(Nb_{1-x}Ta_x)_2O_6$ solid solutions were •OH-dominated reactions. The theoretical calculation demonstrated that the VB level of $Sn(Nb_{0.8}Ta_{0.2})_2O_6$ guarantees a strong potential to oxidize the organic dye, while the CB level supplies the sufficient light absorption, which contributes to its high performance. This work proposes that the study method of combing the photocatalytic mechanism with the theoretical calculation will provide a more effective approach to develop high-efficient photocatalysts.

Acknowledgments

This work was partially supported by the National Basic Research Program of China (No. 2014CB239301); Collaborative Innovation Center of Chemical Science and Engineering (Tianjin). REN Jian thanks Dr. TONG Hua for his kind advice to this work. The authors are grateful to Prof. DU Haiyan for the assistance in the XRD and Ms. HE Fei for the XPS analysis.

Appendix A. Supplementary data

Supplementary data associated with this article can be found, in the online version, at http://dx.doi.org/10.1016/j.apcatb.2014.12.021.

References

[1] M.R. Hoffmann, S.T. Martin, W. Choi, D.W. Bahnemann, Chem. Rev. 95 (1995) 69–96.
[2] A. Kudo, Y. Miseki, Chem. Soc. Rev. 38 (2009) 253–278.
[3] H. Tong, S. Ouyang, Y. Bi, N. Umezawa, M. Oshikiri, J. Ye, Adv. Mater. 24 (2012) 229–251.
[4] A. Houas, H. Lachheb, M. Ksibi, E. Elaloui, C. Guillard, J.-M. Herrmann, Appl. Catal. B – Environ. 31 (2001) 145–157.
[5] M. Pelaez, N.T. Nolan, S.C. Pillai, M.K. Seery, P. Falaras, A.G. Kontos, P.S.M. Dunlop, J.W.J. Hamilton, J.A. Byrne, K. O'Shea, M.H. Entezari, D.D. Dionysiou, Appl. Catal. B: Environ. 125 (2012) 331–349.
[6] S. Rodrigues, K.T. Ranjit, S. Uma, I.N. Martyanov, K.J. Klabunde, Adv. Mater. 17 (2005) 2467–2471.
[7] J. Yu, Q. Xiang, M. Zhou, Appl. Catal. B: Environ. 90 (2009) 595–602.
[8] R. Asahi, T. Morikawa, T. Ohwaki, K. Aoki, Y. Taga, Science 293 (2001) 269–271.
[9] S.U.M. Khan, M. Al-Shahry, W.B. Ingler, Science 297 (2002) 2243–2245.
[10] S. Sakthivel, H. Kisch, Angew. Chem. Int. Ed. 42 (2003) 4908–4911.
[11] Z. Zou, J. Ye, K. Sayama, H. Arakawa, Nature 414 (2001) 625–627.
[12] D. Wang, J. Ye, T. Kako, T. Kimura, J. Phys. Chem. B 110 (2006) 15824–15830.
[13] S. Ouyang, N. Kikugawa, Z. Zou, J. Ye, Appl. Catal. A: Gen. 366 (2009) 309–314.
[14] Z. Zou, J. Ye, H. Arakawa, Chem. Mater. 13 (2001) 1765–1769.
[15] J. Tang, Z. Zou, J. Ye, Chem. Mater. 16 (2004) 1644–1649.
[16] Z. Yi, J. Ye, N. Kikugawa, T. Kako, S. Ouyang, H. S-Williams, H. Yang, J. Cao, W. Luo, Z. Li, Y. Liu, R.L. Withers, Nat. Mater. 9 (2010) 559–564.
[17] D. Wang, J. Ye, H. Kitazawa, T. Kimura, J. Phys. Chem. C 111 (2007) 12848–12854.
[18] K. Maeda, K. Teramura, D. Lu, T. Takata, N. Saito, Y. Inoue, K. Domen, Nature 440 (2006) 295.
[19] W. Wang, F. Huang, X. Lin, Scripta Mater. 56 (2007) 669–672.
[20] D. Wang, T. Kako, J. Ye, J. Am. Chem. Soc. 130 (2008) 2724–2725.
[21] S. Ouyang, J. Ye, J. Am. Chem. Soc. 133 (2011) 7757–7763.
[22] Y. Liu, W.J. Son, J. Lu, B. Huang, Y. Dai, M.H. Whangbo, Chem. Eur. J. 17 (2011) 9342–9349.
[23] H. Kato, A. Kudo, Chem. Phys. Lett. 295 (1998) 487–492.
[24] A. Kudo, S. Nakagawa, H. Kato, Chem. Lett. (1999) 1197–1198.
[25] J. Ye, Z. Zou, A. Matsushita, Int. J. Hydrogen Energy 28 (2003) 651–655.
[26] D. Li, N. Xu, Y. Chen, Z. Zou, Res. Chem. Intermed. 31 (2005) 521–527.
[27] T. Xu, X. Zhao, Y. Zhu, J. Phys. Chem. B 110 (2006) 25825–25832.
[28] X. Lin, F. Huang, W. Wang, Y. Wang, Y. Xia, J. Shi, Appl. Catal. A: Gen. 313 (2006) 218–223.
[29] Y. Zhang, C. Liu, G. Pang, S. Jiao, S. Zhu, D. Wang, D. Liang, S. Feng, Eur. J. Inorg. Chem. 2010 (2010) 1275–1282.
[30] S. Liang, R. Liang, L. Wen, R. Yuan, L. Wu, X. Fu, Appl. Catal. B: Environ. 125 (2012) 103–110.
[31] S. Liang, S. Zhu, Y. Chen, W. Wu, X. Wang, L. Wu, J. Mater. Chem. 22 (2012) 2670–2678.
[32] H. Fu, C. Pan, W. Yao, Y. Zhu, J. Phys. Chem. B 109 (2005) 22432–22439.
[33] X. Yang, L. Xu, X. Yu, Y. Guo, Catal. Commun. 9 (2008) 1224–1229.
[34] X. Zhang, X. Liu, C. Fan, Y. Wang, Y. Wang, Z. Liang, Appl. Catal. B: Environ. 132 (2013) 332–341.
[35] K. Lv, Y. Xu, J. Phys. Chem. B 110 (2006) 6204–6212.
[36] R. Palominos, J. Freer, M.A. Mondaca, H.D. Mansilla, J. Photochem. Photobiol. A: Chem. 193 (2008) 139–145.
[37] H. Kominami, A. Furusho, S. Murakami, H. Inoue, Y. Kera, B. Ohtani, Catal. Lett. 76 (2001) 31–34.
[38] J.P. Perdew, K. Burke, M. Ernzerhof, Phys. Rev. Lett. 77 (1996) 3865–3868.
[39] S.L. Dudarev, G.A. Botton, S.Y. Savrasov, C.J. Humphreys, A.P. Sutton, Phys. Rev. B 57 (1998) 1505–1509.
[40] P.E. Blöchl, Phys. Rev. B 50 (1994) 17953–17979.
[41] G. Kresse, J. Furthmüller, Phys. Rev. B 54 (1996) 11169–11186.
[42] Z. Yi, J. Ye, Appl. Phys. Lett. 91 (2007) 254108.
[43] G. Li, T. Kako, D. Wang, Z. Zou, J. Ye, J. Solid State Chem. 180 (2007) 2845–2850.
[44] Y. Hosogi, Y. Shimodaira, H. Kato, H. Kobayashi, A. Kudo, Chem. Mater. 20 (2008) 1299–1307.
[45] B. Serrano, H. de Lasa, Chem. Eng. Sci. 54 (1999) 3063–3069.
[46] L.J. Sham, M. Schlüter, Phy. Rev. Lett. 51 (1983) 1888.